Angel Pérez Santiago, Sadoth Sandoval Torres*, Angélique Léonard, Erwan Plougonven, Mario Díaz-González and Emilio Hernández-Bautista

# Numerical simulation and microtomography study for drying a deformable isodiametric-cellular food

https://doi.org/10.1515/ijfe-2021-0108
Received April 9, 2021; accepted August 29, 2021;
published online September 13, 2021

**Abstract:** The aim of this work is the simulation of volumetric strain of tuberous crop during drying. We propose a poroelastic model for predicting the drying kinetics and volume loss of potato cubes during convective drying. The Biot's theory of poroelasticity was used, which considers the Lamé parameters, Young's modulus and Poisson's ratio. Drying kinetics and volumetric strain were modeled and compared versus experimental data. An X-ray microtomograph coupled with image analysis was used to visualize the shape and size of the samples during drying. Drying experiments were conducted at 50, 60 and 70 °C, 20% RH, with an air velocity of 1 and 2 m/s. The drying process was interrupted several times to perform tomographic acquisitions. We found a period of ideal shrinkage, nevertheless, the volumetric strain reveals a kinetic behavior over time. The model computes the volumetric strain, which describes correctly the experimental data obtained by microtomography.

**Keywords:** Darcy's law; Lamé parameters; microtomography; stress-strain; volumetric strain.

## 1 Introduction

Industry has a real interest to predict and control the texture of plant-based foods, particularly in relation to processing and/or postharvest treatments [1], and due to a huge and ever-increasing range of foods, manufacturers find themselves in an intensely competitive scenario [2]. The quality of foods is of primary importance for the food industry and to consumers [3]. Also, due to an increasing refusal in the use of chemicals as food preservatives, an improved quality of the dried product is required in drying operations [4, 5]. The food industry needs the development of new products, processes, and equipment in order to boost the quality and safety. As new ingredients, processes, and equipment are tested, the predictive capacity of models can play a considerable role [6, 7].

Convective drying is a complex process that targets the reduction of moisture content in materials by using a warm airflow. In convective drying, the drying rate is generally high at the beginning of the process since it depends largely on the concentration of moisture at the surface of the product [5]. The removal of water modifies the food microstructure, and in some materials allows chemical reactions [8, 9].

Foods undergo volumetric changes during the drying process, nevertheless most research works neglect the deformation of materials [10]. These changes are accompanied by internal strain-stress formation, resulting in inferior product quality [11]. Mayor and Sereno [12] notes that the loss of water and heating cause stresses in the cellular structure of the food, allowing a change in shape and dimension, and Fanta et al. [13] explains the shrinkage results from the collapse of cells during water evaporation, which has a negative effect on the quality of the material.

Efforts to understand and simulate food deformation during drying are necessary in order to enhance food quality and food operations. The numerical simulations predict the behavior of materials under different scenarios. The properties and responses of the material can be visualized prior to experiments, in this way, we can quantify the magnitude of the changes. In the case of drying, the simulations are useful since we can predict the magnitude of the volume loss and the evolution of the elastic modulus. In addition, the simulations reduce the experimental testing and reengineering costs. Dhall and Datta [14], developed a model for deformable food. Assuming the solid skeleton is an incompressible hyperelastic material,

***Corresponding author: Sadoth Sandoval Torres**, Instituto Politécnico Nacional, CIIDIR Oaxaca, Hornos 1003, Santa Cruz Xoxocotlán, Oaxaca, C.P. 71230, México,
E-mail: ssandovalt@ipn.mx. https://orcid.org/0000-0001-8518-1362
**Angel Pérez Santiago,** Instituto Politécnico Nacional, CIIDIR Oaxaca, Hornos 1003, Santa Cruz Xoxocotlán, Oaxaca, C.P. 71230, México. https://orcid.org/0000-0002-6644-7142
**Angélique Léonard and Erwan Plougonven,** Chemical Engineering, University of Liège, Liége, Belgium
**Mario Díaz-González and Emilio Hernández-Bautista,** Instituto Politécnico Nacional, CIIDIR Oaxaca, Hornos 1003, Santa Cruz Xoxocotlán, Oaxaca, C.P. 71230, México; and Tecnológico Nacional de México/Instituto Tecnológico de Oaxaca, Oaxaca de Juarez, México

they used a Neo-Hookean model. Their model was validated with experimental data for convective drying of potato slabs obtained from ref. [15]. The shrinkage was computed as a percentage changes in thickness, length and width of the potato samples. They found a linear relationship between moisture content and shrinkage, observing shrinkage of potato slabs stops below a critical moisture content. Curcio and Aversa [16] proposed a mechanical model for potato cylinders assuming an anisotropic change. An air velocity of 2.2 and 2.8 m/s, temperatures of 70 and 85 °C, and a relative humidity between 35 and 50% were applied by using a cylindrical drying cell. The authors consider the potato follows an elastoplastic behavior, then the stress–strain relationship was expressed through the elastoplastic stress–strain matrix. The authors use a vernier caliper to measure the dimensions of the sample, and predict the shrinkage of the thickness and diameters of potato samples with a maximum deviation of 10%.

Another approach developed in the last years analyzes the mass and heat transport in deformable media by considering the Biot's theory of poroelasticity. This perspective studies the behavior of materials whose porous microstructures are occupied by a fluid. This approach has been applied in systems like geomaterials, biomaterials, gels, and polymers, but rarely in foods [14, 17]. In a deformable porous material, the deformation of the solid skeleton is mechanically coupled to the flow of the interstitial fluids. For simplicity, only two phases, solid and fluid, are considered. The poroelasticity theory combines Darcy's law with Terzaghi's effective stress and nonlinear elasticity in a rigorous kinematic framework [18].

Usually, measuring shrinkage from drying involves destructive or inaccurate techniques such as volume displacement methods [19]. The impact of drying methods on the food microstructure, to our knowledge, remains to be studied, even though it is a crucial aspect in food quality [20]. X-ray computed tomography (CT) is a technique that uses differences in X-ray absorption to generate attenuation maps of samples. From multiple radiographs taken at different angles, a 3D image is reconstructed or computed. Due to its nondestructive nature, it has become a useful tool for exploring the internal structure of food materials. Many researchers use X-ray CT to characterize different plant-based food materials, including apple [21], kiwi [22], raspberry [23], mango [24], beetroot [25] and banana [26]. This non-destructive technique is emerging in the field of food science [20]. It has been successfully utilized to investigate frozen apples [27], fried potatoes [28], and dried banana slices [19].

The aim of this work is the simulation of drying of potatoes (*Solanum tuberosum*) undergoing deformation. Based on thermodynamic and phenomenological principles, the drying model implements the poroelastic theory coupled to heat and mass transfer. We consider the Biot-Willis coefficient, the specific storage coefficient and the Lamé parameters. Our model predicts the volume loss and drying kinetics based on continuum mechanics. The numerical results are validated for the first time with experimental results obtained from CT.

# 2 Materials and methods

The potato variety Alpha (*S. tuberosum*) was obtained from a local supermarket in Liège (Belgium) and stored at 3–4 °C for one to two days. The initial moisture content was determined according to the oven-dry method (AOAC 32.1.03) [29].

The effectiveness of the proposed models was evaluated by the Root Mean Square Error (RMSE), which is a standard way to measure the error of a model in predicting quantitative data:

$$\mathrm{RMSE} = \sqrt{\frac{1}{N}\sum_{z=1}^{N}(S_z - O_z)^2} \tag{1}$$

## 2.1 Drying experiments

Drying by forced convection was performed at controlled conditions. Potato cubes (edges of 0.018 m) were prepared. The initial volume of the cubes was 5.832E-6 $m^3$. The samples were dried at three temperatures (50, 60 and 70 °C), with a relative humidity of 20% and air velocity of 1, and 2 m/s. Cubes were dried in a micro dryer, as described in previous studies [30]. The micro-dryer can operate at temperatures ranging from 20 to 180 °C. In this dryer, the air flow ranges from 0.3 to 5 m/s. The maximum steam production at the highest air flow achieves an absolute humidity of about 0.2 kg/kg of dry air.

The samples were placed in a tray. The potato lies in the drying chamber on a supporting grid linked underneath to a precision weighing device (BP 150 from Sartorius, Germany; accuracy: 0.001 g). During drying, the mass of the potato cube sample was recorded every 30 min for the first 2 h, then every 1 h for the next six, and every 2 h after that when necessary. The weighing device is connected to a PC that records the mass.

## 2.2 X-ray microtomography

The microtomograph used in this study was a Skyscan-1074 (Skyscan, Belgium). The X-ray source was set at 40 kV and 1 mA. The detector was a 2D, 768 × 576 pixels, 8 bit X-ray camera with a spatial resolution of 41 µm, as described in ref. [31]. Radiographs were taken, with a 900 ms exposure time, every 3.6° over 180°. CT acquisitions were interlaced with mass measurements during drying.

## 2.3 Image analysis

After scanning, CT reconstruction was performed using Skyscan's NRecon software (v. 1.6.9.8), generating a 3D grayscale X-ray attenuation map of the sample. Simple thresholding was used to binarize the image, assigning each pixel to either the sample or void. A simple connected component analysis of the void phase can highlight the closed pores inside the potato. Sample volume was measured through pixel counting in the FIJI software (Figure 1).

## 2.4 Fundamentals for the mathematical model and simulations

The following assumptions were considered in this work: (1) the potato is supposed isotropic (considering the nearly isodiametric cells [32], (2) the solid, liquid, and vapor phases are continuous, so a representative volume element can be used, (3) the water vapor-dry air mixture is an ideal gas, (4) The phases are in thermodynamic equilibrium, meaning the temperature is the same on the entire interface, (5) air is insoluble in liquid, (6) the liquid water in the pores is incompressible. Deformation implies a change in the distance between two points in the material, and is defined as the relative deformation, i.e., the change in distance (e.g., length of a specimen) divided by the original distance; then it could be displayed as a dimensionless quantity [33]. We have assumed domain stresses are impacted by the solid matrix and fluid, and we have represented the displacements as a function of stress through Lamé-Hooke equations. Potatoes are considered as a poroelastic material, then the relation between the stress tensor and the strain tensor is written in terms of the Lamé constants. The geometric domain is a cube with edge 0.018 m.

**2.4.1 Conservation equations:** The change in moisture content is explained by the migration of free and vapor water, and the effect of contraction, according to Eq. (2).

$$\frac{\partial W}{\partial t} + \frac{1}{\rho_s}\left(\nabla \cdot n_l + \nabla \cdot n_v + \nabla \cdot n_\sigma\right) = 0 \tag{2}$$

The flow of liquid is written in terms of a concentration gradient [34], where the permeability of the tissue is taking into account. The liquid flow can be written as:

$$n_l = \begin{cases} -D_c \nabla c_l & , \quad W \geq W_c \\ 0 & , \quad W < W_c \end{cases} \tag{3}$$

$D_c$ is the capillary diffusivity (not molecular diffusivity) of water through the cell. In practice, $D_c$ is treated as effective diffusivity, which includes the liquid pressure provoked by a concentration difference, as proposed by [14]:

$$D_c = \rho_l \frac{k_{\text{eff}}}{\mu_l} \frac{\partial p_l}{\partial c_l} \tag{4}$$

The transport mechanism for the moisture transfer during the capillary phase is explained by Darcy's Law. The driving force responsible for the capillary flow is the pressure gradient of the liquid phase. The retention of water is a result of attractive forces between the solid and liquid phases [35]. The stresses are a consequence of the internal pressure variation within the material during convective drying, provoked by an evacuation of liquid water, mainly. Mathematically, this contribution is expressed as:

$$n_\sigma = -\frac{\rho k_l}{\epsilon_p S_l \mu_l} \nabla P_l \tag{5}$$

Where liquid pressure and saturation have an important effect on stress. The expression for liquid saturation is as follows:

$$S_l = \frac{W \cdot \rho_s (1-\phi)}{(1-W)\epsilon_p \cdot \rho_l} \tag{6}$$

The transport of water vapor is described by a combination of the Fick's law and Darcy's law, as shown in Eq. (6). The gas transport is calculated by using an effective diffusion coefficient [36].

$$n_v = \begin{cases} 0, W \geq W_c \\ -\rho_g D_{\text{eff}} \nabla X_v = -\rho_g D_{\text{eff}} \nabla \left(\frac{P_v}{P_g}\right), \quad W < W_c \end{cases} \tag{7}$$

For the macroscopic dry air conservation, we write:

$$\frac{\partial \rho_a}{\partial t} + \nabla \cdot (n_a) = 0 \tag{8}$$

The flux of dry air is described as follows:

$$n_a = \begin{cases} 0, W \geq W_c \\ -\rho_g D_{\text{eff}} \nabla X_a = -\rho_g D_{\text{eff}} \nabla \left(\frac{P_a}{P_g}\right), \quad W < W_c \end{cases} \tag{9}$$

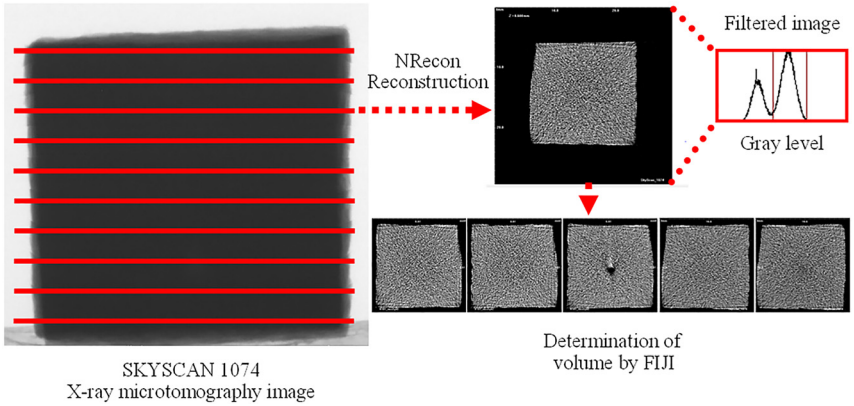


**Figure 1:** Methodology for volume estimation.

For the energy conservation, we have:

$$\rho C_p \frac{\partial T}{\partial t} + \rho_i C_{p_i} n_i \cdot \nabla T + \nabla \cdot (K \nabla T) + \lambda(n_v) = 0 \tag{10}$$

In order to compute the volumetric strain ($e_{\text{vol}}$) (Eq. (11)), we consider the stress tensor ($\sigma$), the Biot-willis coefficient, the drainage coefficient ($S$), and a coupling with the Darcy's law (Eq. (12)). The loss of a fluid phase affects the normal stress, in this way, we use the Darcy's law to estimate the flow field in the model.

$$\rho S \frac{\partial \sigma_f}{\partial t} + \nabla \cdot \left( -\frac{\rho k}{\mu} \nabla \sigma_{pl} \right) + \rho \alpha_B \frac{\partial e_{\text{vol}}}{\partial t} = 0 \tag{11}$$

$$\frac{\partial \sigma_{pl}}{\partial t} + \nabla \cdot \left( -\frac{\rho k}{\mu} \nabla n_\sigma \right) = 0 \tag{12}$$

The model considers the rate of change in strain from the solid-deformation equations coupled to the fluid pressure gradient. Hence, we can write an equation that relates the fluid stresses and the material deformation. The stress-strain equation (Eq. (11)) involves two relevant poroelastic parameters: the Biot-Willis coefficient ($\propto_B$) which translates the efficiency of fluid pressure to counterbalance the total stress applied, and the specific storage coefficient ($S$) characterizing the amount of fluid evacuated by the decreasing pressure. Equation (11) considers the volume loss, $\frac{\partial e_{\text{vol}}}{\partial t}$ being the volumetric strain of the porous matrix. The rate of change in strain $\frac{\partial e_{\text{vol}}}{\partial t}$ acts as a coupling term in Darcy's Law (Eq. (12)) and becomes quasi-static when solved simultaneously with a time-dependent flow model.

The governing equation for the poroelastic material model is:

$$-\nabla \cdot \sigma_f = \rho \cdot g \tag{13}$$

The poroelastic material model uses Eq. (11) to describe changes in the total stress tensor and porous matrix displacement due to boundary conditions and changes in pore pressure. Equation (13) describes a state of static equilibrium because the changes in the solid balance out immediately, that is, there are no time-dependent terms. Likewise, specific storage coefficient is expressed as:

$$S = \epsilon_p \cdot \chi_f + \frac{(\alpha_B - \epsilon_P)(1 - \alpha_B)}{\text{K}} \tag{14}$$

The 3D constitutive relation between the stress tensor σ and the strain tensor can be conveniently written in terms of the Lamé constants. The Lamé's constant $\boldsymbol{\lambda}_s$, and the shear modulus $\mu_s$, are related to Poisson's ratio $v$, and elastic modulus $E$. Poisson's ratio, $v$, is defined as the ratio of lateral strain to axial strain in a specimen subjected to axial deformation; for porous materials $v$ tends to zero. It is a constant that relates modulus of rigidity to Young's modulus, expressed as the following equation:

$$E = 2G(v + 1) \tag{15}$$

We chose a value of 0.3 for the Poisson's ratio to characterize the mechanical property of potatoes in the glassy state. The elastic modulus, $E$, has been estimated as a function of moisture content (dry basis) and is given by [37]:

$$E = 1.691 \cdot 10^7 \text{e}^{-0.522 \cdot \text{W}} \qquad W > 1.0 \tag{16}$$

$$E = 5.23 \cdot 10^7 \text{e}^{-1.704 \cdot \text{W}} \qquad W \leq 1.0 \tag{17}$$

A study in Golden Delicious apples, reveals a linear relationship between Young's modulus and the Lamé's coefficient [38].

**2.4.2 The initial and boundary conditions:** The initial moisture content (average) was 5.47 kg water/kg dry matter, and the temperature at $t = 0$ was 22 °C. The fluxes at the surfaces are calculated by using the heat and mass transfer coefficients and the corresponding potentials. There are six boundary conditions called CF1, CF2, CF3, CF4, CF5 and CF6 (face on a supporting grid), which are initially considered at the same temperature. Equation (18) represents the outward flow of water vapor leaving the material.

$$-n \cdot D_{\text{eff}} \nabla W\big|_{\text{CF1–CF6}} = \frac{1}{\rho_s} h_m (C_{v\infty} - C_v^g) \tag{18}$$

To solve the dry-air mass equation, we applied a Neumann boundary condition (Eq. (19)) in order to estimate the mass flux. The mass transfer coefficient km (m $s^{-1}$) was calculated from the correlation for the Sherwood number. Equation (20) is used for forced convection on a flat plate with laminar flow,

$$\rho_a|_{\text{CF1–CF6}} = \rho_{a\infty} \tag{19}$$

$$Sh = 0.66 \text{Re}^{1/2} Sc^{1/3} \quad 0.6 \leq Sc \leq 50 \tag{20}$$

For the energy equation, the boundary condition is expressed by Eq. (21). We have calculated the coefficients of heat and mass transfer from experimental data.

$$-n \cdot k \nabla T|_{\text{CF1–CF6}} = h_c (T_\infty - T_s) - \lambda [h_m (C_{v\infty} - C_v^g)] \tag{21}$$

The heat transfer coefficient (W $m^{-2}$ $K^{-1}$) was calculated from the Nusselt number (Eq. (22)).

$$\text{Nu} = 0.66 \text{Re}^{1/2} \text{Pr}^{1/3} \quad \text{Pr} \leq 1 \tag{22}$$

To solve the poroelastic Eq. (10), we consider the interaction between the solid phase and the pressure of the air surrounding the material and the tension produced by the loss of moisture content, then we write:

$$\sigma_f\big|_{\text{CF1–CF5}} = P_\infty + \sigma_{\text{AMS}} \tag{23}$$

$$u, v, w|_{\text{CF6}} = \text{free} \tag{24}$$

The input parameters of the model are listed in Table 1.

The model was solved by implementing the conservative equations in COMSOL Multiphysics 4.3b (Comsol Inc., Burlington, MA). A Lagrange frame was used as reference using quadratic shape functions. The equations for moisture conservation (Eq. (2)), dry air conservation (Eq. (8)) and energy conservation (Eq. (10)), were solved in the Coefficient Form PDE, Eq. (11) was solved by using the poromechanics module and Eq. (12) was solved by using the Darcy module. A meshing of 100 tetrahedral elements and 84 triangular elements were implemented. The direct solver MUMPS was used. The poroelastic model equations were solved by the finite element method, using a time step of 100 s and 0.01 of relative tolerance.

# 3 Results and discussion

## 3.1 Simulation of drying kinetics and Young's modulus

The averaged initial moisture content of the potato (*S. tuberosum)* was 5.58 *(dry basis)*. The simulations

**Table 1:** Parameters.

| Parameter | Expression | Reference |
|---|---|---|
| Thermal conductivity (W/m·K) | $k = 0.276 + 0.293 \log(M)$ | [39] |
| Latent heat of vaporization (kJ/kg) | $\lambda = 2501.3 - 2.301T - 0.00142T^2$ | [40] |
| Heat capacity (Cal/g K) | $C_p = 0.008W + 0.20$ | [41] |
| Effective diffusivity coefficient ($m^2/s$) | $D_{\text{eff}} = a \exp\left(\frac{b}{T}\right) \exp\left(\frac{c}{M}\right)$ | [42] |
| Saturated vapor pressure (Pa) | $P_{\text{vsat}} = 100\exp\left[20.9006 - \frac{5204.9}{T_a}\right]$ | [43] |
| Vapor concentration on the surface ($kg/m^3$) | $C = 2.166 \times 10^{-3}\left(\frac{P_{\text{vsat}}}{T_{\text{sup}}}\right)$ | [15] |
| Water density ($kg/m^3$) | $\rho_w = 1000$ | |
| Dry solid density ($kg/m^3$) | 1071 | [44] |
| Initial moisture content (dry basis) | 5.47 | Experimental |
| Permeability (m2) | $4.168 \times 10^{-12}$ $m^2$ | [45] |
| Poisson's ratio | $0 < v < 0.5$ | [32, 46–48] |

represent the drying kinetics at different drying conditions. In Figure 2, we show the numerical predictions, the experimental drying kinetics, and the Root Mean Squared Error (RMSE) for each experiment. We observe the simulations predict with high accuracy the experimental data. As drying temperature increases the drying time decreases, likewise a higher airflow improves the loss of moisture content. Initially, the pores are saturated with free water until behaving as a hygroscopic material. The drying periods are theoretically separated by a critical moisture content. The critical moisture content (Wc) indicates the beginning of the hygroscopic domain in the model, where the water activity (aw) plays an important role. The critical moisture content commonly varies with the thickness of the material and the external drying conditions [49]. In this work the critical moisture content was 1.0 *(dry basis)*.

The shape of the kinetics was influenced by temperature and airflow velocity. The drying time was reduced when samples were exposed to a higher airflow velocity, due to faster drying rate. During drying of foodstuffs, particularly at higher temperatures, a hardening of the surface tissue may develop; this hardened layer (case-hardening) opposes resistance to moisture transport in the cellular layers of inner tissues and deteriorates the rehydration capacity of the samples. In our experiments, a thin dry crust was observed. The crust is linked to the rheological behavior of the solid phase, which strongly depends on the moisture content of the material, in this way, the mechanical behavior of potatoes is depicted in Figure 3. In this figure we observe the Young modulus increases as the material moisture content decreases. It means, drying increases the Young modulus, then it is necessary more stress to cause a deformation in the solid, because of the material is getting drier and stiffer. A strong increase of the Young modulus was observed for the experiment at 70 °C. At the end of drying, a value of $2.7x10^7$ Pa correspond to the sample exposed at 1 m/s airflow, and $3.5 \times 10^7$ Pa to the sample exposed at 2 m/s airflow. In this regard, a drying temperature of 70 °C will not be an appropriate drying condition, because it will hinder the rehydration process.

During drying an intense deformation is experienced, affecting the properties of the solid phase, transitioning from a rubber to glassy state (impacting on the pore network at the surface), and forming a dried shell. Water transport in a cellular material depends on its passage in and around cells. According to ref. [34], intracellular transport occurs when drying at low temperatures (below 52 °C), in this case, moisture migration faces resistance from cell membranes, cell walls and intercellular spaces. Extracellular transport occurs at higher temperatures (above 52 °C), when the cell membrane is broken.

In order to observe the volume changes during drying, we compute the volumetric strain from simulations. Displacements predicted by simulation were in the order of $10^{-6}$ m (quasi-static deformation). Displacements allowed to calculate radial and axial strains.

## 3.2 Volumetric strain simulation

The simulated volumetric strain was obtained from V/V0, where V0 is the initial volume and V is the volume at different times solved by the model (Figure 4). The experimental volumetric strain was computed from the information obtained by microtomography. We noticed the volumetric strain display an ideal linearly behavior, as reported in previous mathematical models [17, 50]. For the first time, the changes in volume at different drying times were experimentally measured from X-ray microtomography images. The simulations predict with high accuracy (RMSE), the decrease of volume of the cubes.

Figure 5a shows the numerical and experimental results of volumetric strain as a function of time for drying at 1 m/s. The results show the kinetic behavior of volumetric

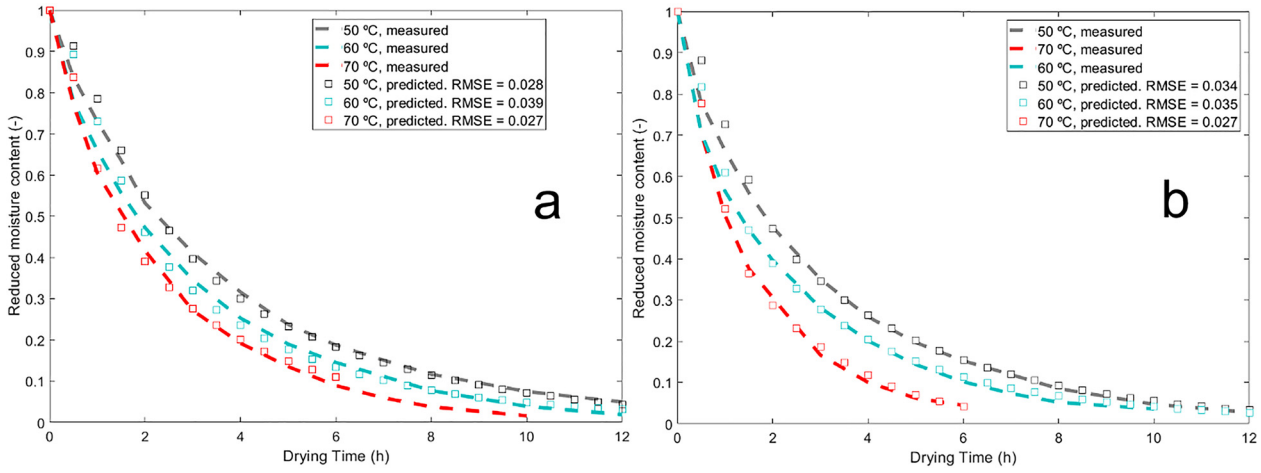


**Figure 2:** Experimental and simulated drying kinetics at three different temperatures (50 °C, 60 °C and 70 °C) and two air flow speeds: (a) 1 m/s, and (b) 2 m/s.

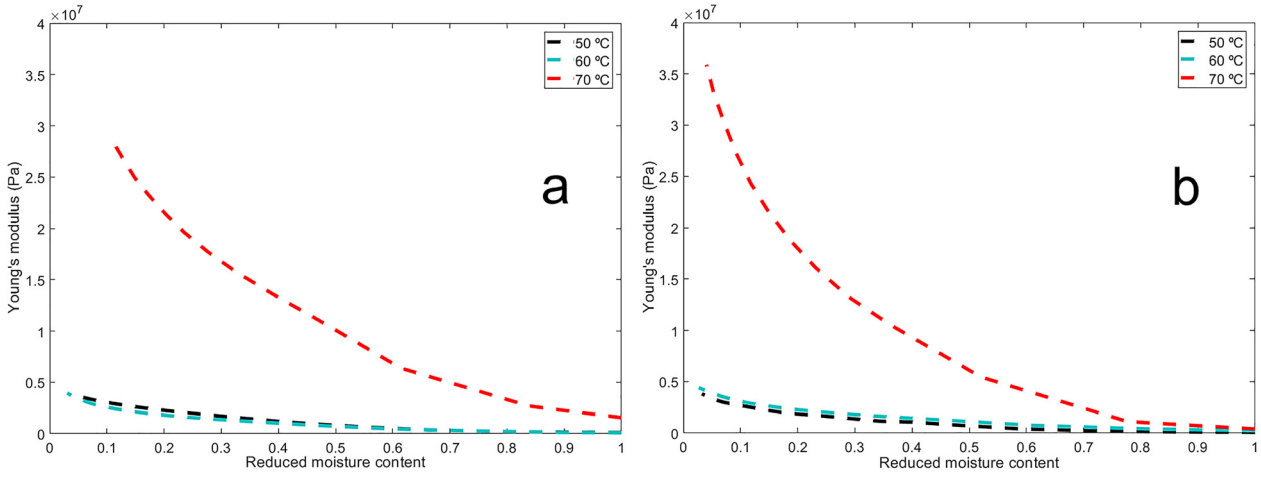


**Figure 3:** Simulated young's modulus at three different temperatures (50 °C, 60 °C and 70 °C) and two air flow speeds: (a) 1 m/s and (b) 2 m/s.

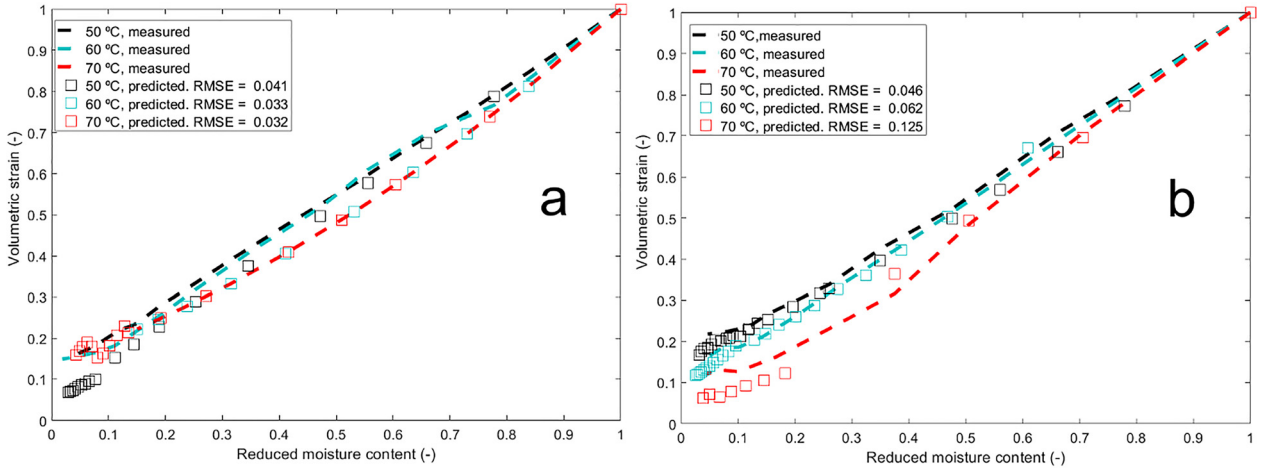


**Figure 4:** Experimental and simulated volumetric strain at three different temperatures (50 °C, 60 °C and 70 °C) and two air flow speeds: (a) 1 m/s and (b) 2 m/s.

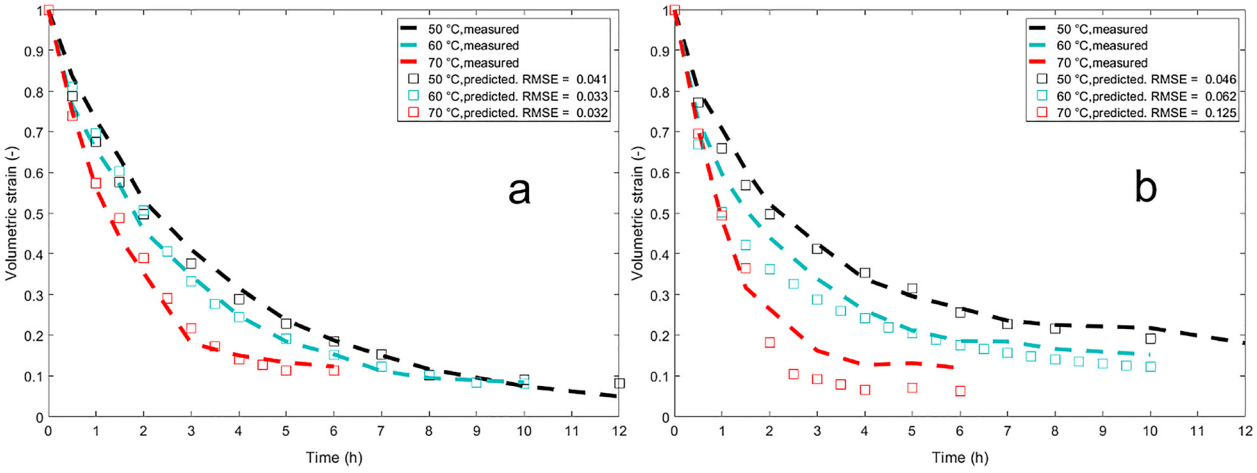


**Figure 5:** Experimental and simulated volumetric strain as a function of time, at three different temperatures (50 °C, 60 °C and 70 °C) and two air flow speeds: (a) 1 m/s and (b) 2 m/s.

strain, which confirms a strong dependence on moisture content. Likewise, it is observed the temperature has an important effect on the contraction, since at 70 °C, the volumetric strains decrease at a higher rate (slope) compared to the experiments at 50 and 60 °C.

Figure 5b shows the results for the experiments at 2 m/s air flow. At 70 °C, the volumetric strain decreases dramatically (red line), and for the experiments at 50 and 60 °C, the values are higher than the experiments at a lower air velocity, which confirms the importance of convective air flow. Poroelasticity describes the interaction between fluid flow and solid deformation, in this way the model can compute the volumetric strain. Poroelasticity is based on the geometrically linear theory. This means that in the strain tensor only linear terms of the displacement gradients are contained, which is well supported by the fact that fluids exert normal forces represented as engineering stress.

We observe that at 1 m/s air flow, the final volume of the samples is similar, however, for the experiments at 2 m/s, it is observed that the final volume is much lower for the sample exposed to an air temperature of 70 °C. The results show that higher airflows cause different shrinkage rates, and a higher volume loss. At higher air flow (2 m/s), the air temperature has an important effect on the final volume of the samples.

The trend for volumetric strain could be related to a loss of liquid water (free water) during the first few hours of drying. This free water exerts a pressure on the pores of the material and provides the stress necessary to preserve a rigid structure. Turgor pressures have an impact on tissue strength, the pressure is exerted by intracellular liquids, whose are transported towards the surface. When the water is removed from the material, the pore network is drained and the solid deforms. In other words, these changes are due to the stresses developed while water is removed from the material, phenomena also observed by Witrowa-Rajchert and Rząca [51].

## 3.3 Microtomography results related to simulations

Figure 6 shows the patterns of deformation and volume loss obtained during the tomographic acquisition. We obtain many scans at different drying times and the experimental volumetric strain was computed from this information. The similarities between these images are an evidence of the pattern of volume loss. As drying occurs the size and shape of the samples are impacted by the heating intensity. X-ray absorption is affected by moisture content, then the gray scale allows to observe drier regions at the surface and in the center. The method visualizes the intensity of volume loss which is computed from the reconstructed 3D images to get the experimental volumetric strain. During drying we observe the formation of air cavities, with a complex morphology. The food deformation is stronger when the amount of evaporated water is larger, which is a function of temperature and air flow, phenomena clearly observed at 70 °C. CT offers new information to understand the pattern of volumetric strain during drying.

Figure 6 shows the shape of the potato cubes and how it evolved when drying. Changes in greyscale in the tomographic reconstructions are linked to solid density and water content. When the drying is further along, volume contraction becomes significant, the cube takes on a

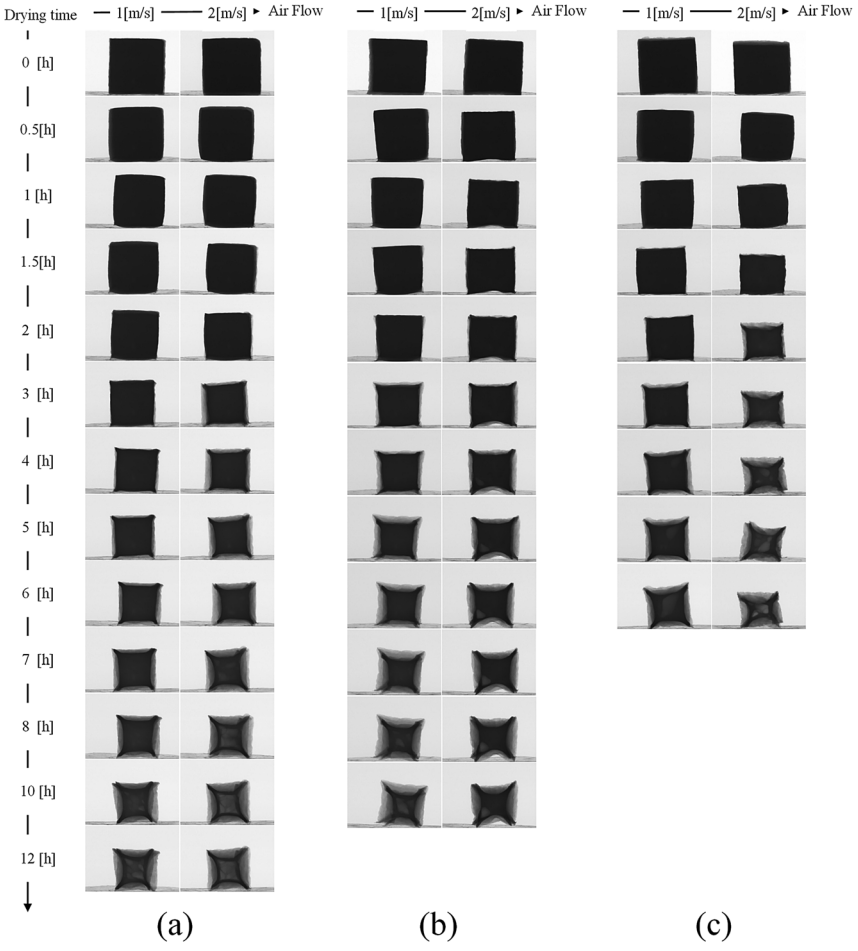


**Figure 6:** Images by X-ray microtomography at different air flow speeds (1 m/s and 2 m/s), and different temperatures: (a) 50 °C, (b) 60 °C and (c) 70 °C.

warped shape, and a non-uniform distribution of pores appears. This occurs at different times depending on drying condition, but the warped shape is well evidenced at the end of the experiments. Figure 6 shows in light gray color the regions of solid phase with less density and lower moisture content. This also occurs in the center of the cube as the density is lower due to the formation of air bubbles and lower moisture content. According to ref. [52], a decrease of the liquid pressure allows the decrease of turgor pressure, linked to the stiffness of the cellular tissue. In this work, we are revealing the pattern of volume loss by using a non-destructive technique.

During drying, the water evaporation at the surface is linked to volumetric strain. In Figure 7, we observe the mass flux as a function of moisture content. The mass flux was more intense for drying condition at 70 °C and 2 m/s airflow. The model predicts the mass flux for all the experiments, a larger mass flux is evidenced at 70 °C. In the first hours of drying, moisture transport is controlled by the external drying conditions, and free water allows a higher drying rate, nevertheless as drying occurs, the internal conditions control the moisture migration, in this way, the microstructure impacts the pathway of moisture migration and drying rate decreases.

In order to observe the internal structure of the samples, cross-sections images of CT are presented in Figure 8. The images correspond to four cuttings (slices) showing the transversal structure of the sample. S1, S2, S3 and S4 represents the different cuttings, in black color we observe the air cavities and in light gray the solid structure. The ability to measure and visualize food microstructure in 3D is important to understand the food deformation in association with drying conditions. Images reveal the internal disorder and irregular shape of air cavities. The water vapor interacts with the solid phase displacement, forming air bubbles difficult to quantify.

The collapse of the tissue structure results in cavity formation, a heterogeneous pattern is observed at different drying conditions. Figure 8 shows the evidence on the formation of cavities by displaying cross-sectional cuts at different drying times. The phenomenon is complex, and cavities appears at different drying times with different patterns. At the end of drying, for experiments at 50 °C, we observe larger cavities for condition at 2 m/s airflow; for

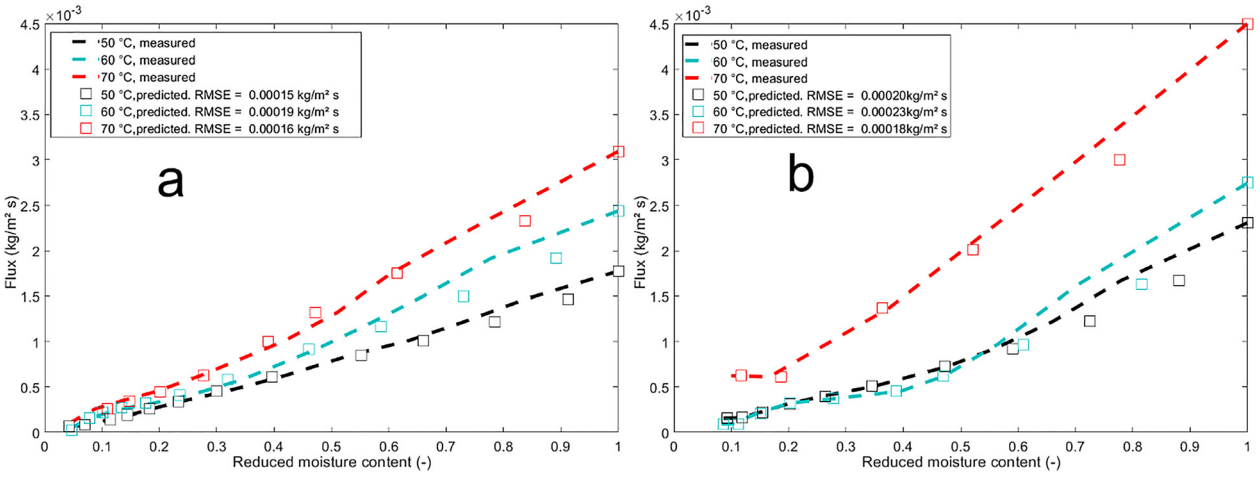


**Figure 7:** Experimental and simulated mass flux at different temperatures (50 °C, 60 °C and 70 °C) and two air flow speeds: (a) 1 m/s and (b) 2 m/s.

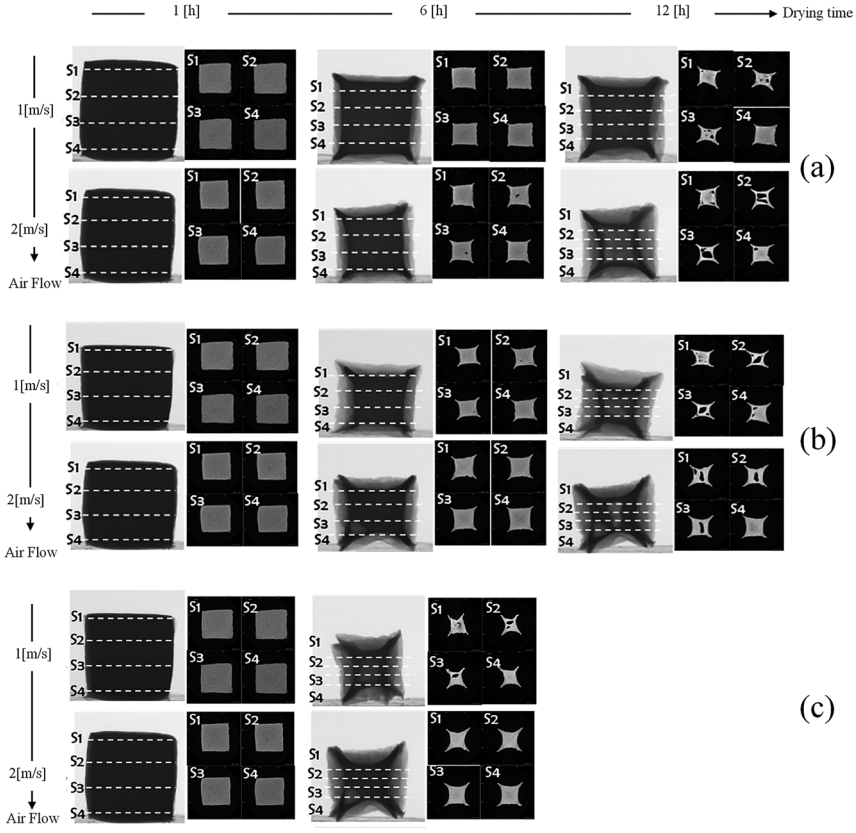


**Figure 8:** Cross-sections images by X-ray microtomography. Experimental data at two air flow speeds: 1 m/s and 2 m/s, and three different temperatures: (a) 50 °C, (b) 60 °C and (c) 70 °C.

drying at 60 °C the cavities seem to be larger for samples exposed at 1 m/s airflow, and for drying at 70 °C the cavities were observed only for the samples exposed at 1 m/s airflow. The algorithm allows us to compute the external volume loss, nevertheless a further analyze should be implemented in order to compute the internal volume of cavities.

During drying, water vapor migrates within porous media and leaves the surface of food at different evaporation rates. The pressure of water vapor depends on temperature and moisture content. Under constant drying conditions, the surface of the food attains the wet-bulb temperature if heat transfer is driven by convection. Figure 9 depicts the evolution of vapor pressure for each

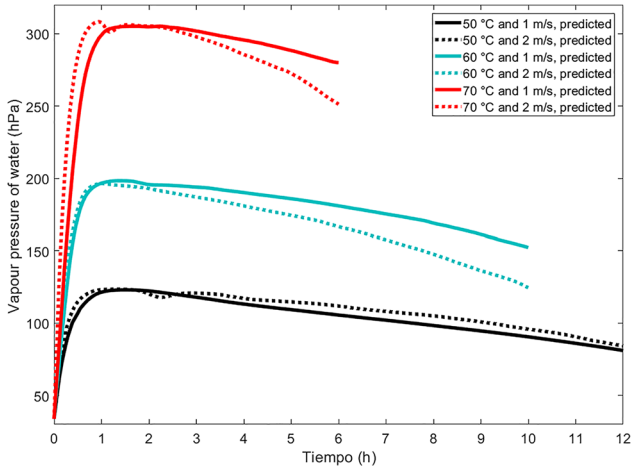


**Figure 9:** Simulation of the water vapor pressure at three temperatures (50 °C, 60 °C and 70 °C) and two air flow speeds: 1 m/s and 2 m/s.

experiment. In the first minutes of drying an increase of gas pressure is observed, since the material is in the heating stage and a large amount of free moisture is available, after that, a maximum vapor pressure is reached because of the food is near from the temperature of airflow. Finally, a decrease of water vapor pressure is evidenced for all the experiments, explained by a lower availability of moisture content. During convective drying the evaporation front recedes at different rates and is influenced by temperature and airflow. As drying temperature increases, the front recedes faster into the food. This is because the higher air temperature provides a higher drying potential and improves the heat flux, but allows a stronger contraction.

Data reveals as the airflow velocity increases, the moisture removal is improved, mainly due to the higher dry air replacement in the food surface, in this way the evaporation front recedes strongly. As drying proceeds, the internal resistance of the product increases, resulting in a falling drying rate and the formation of cavities.

## 4 Conclusions

In this work, a poroelastic model for drying was solved to simulate the drying kinetics and the volumetric strain of potato cubes. The numerical simulations predict adequately the experimental data obtained by the drying experiments and microtomography. The drying kinetics and the volumetric strain (deformation) are impacted by temperature and airflow. The mass flux and the vapor pressure were also computed.

The elastic modulus increases as drying occurs, making the potato cubes stiffer. For the experiment at 70 °C, a strong increase of the young's modulus was evidenced, such situation is inconvenient for potatoes cubes, since the further rehydration process will be inhibited. Also, the results show as airflow velocity increases the young's modulus increases.

The computation of solid displacement allows the estimation of volume evolution during drying. The numerical results show a linear relationship between volumetric strain and the moisture content, nevertheless, the volumetric strain reveals a kinetics behavior when it is plotted as a function of time. The volumetric strain was more intense for the samples exposed at 70 °C, and 2 m/s airflow.

For the first time, X-ray microtomography shows the evolution of the shape and volume of potato cubes during the experiment. We observe the patterns of volume contraction, also the complex, non-uniform and warped shape of the samples. From these images, it was possible to compute the experimental volumetric strains and confirm the linear relationship with moisture content and the kinetic behavior of volumetric strain over the time.

Due to the isotropic nature of the material, a complex pattern of the shape is evidenced. With the 3D advantage and the ability to visualize the internal structure, improved knowledge of dried materials can result in a better understanding of the drying impacts on the fruit and vegetable volume. Cross-sectional cuttings reveal the formation of cavities, nevertheless a methodology to quantify the air cavities must be implemented.

The contraction and volume are important characteristics for potatoes. In this work the evolution of volumetric strain was revealed by simulation and CT, and the simulations show a good accuracy. Smart drying technologies must be implemented in order to reduce the collapse, such technologies must involve the thermal phenomena coupled to non-invasive techniques. In the future, the model should consider both the crust formation and the air cavities in the samples, in order to enhance the comprehension of the impact of drying conditions on these characteristics. Furthermore, an MRI technique could be useful to complement the CT information. The approach can be implemented for other fruits and vegetables.

## Nomenclature

| | |
|---|---|
| $W$ | Moisture content (kg water/kg dry matter) |
| $t$ | Time (s) |
| $\rho$ | Density (kg/m$^3$) |
| $n_l$ | Liquid flux (kg/m$^2$ s) |

| | |
|---|---|
| $n_v$ | Vapor flux (kg/m$^2$ s) |
| $n_\sigma$ | Shrinkage flux (kg/m$^2$ s) |
| $C_p$ | Specific heat (J/kg K) |
| $T$ | Temperature (°C) |
| $K$ | Thermal conductivity (W/m K) |
| $\lambda$ | Coefficient of thermal conductivity of wood (W/m K) |
| $n_a$ | Air flux (kg/m$^2$ s) |
| $S$ | Drainage coefficient (–) |
| $\sigma_f$ | Total stress tensor |
| $k$ | Permeability (m$^2$) |
| $\mu$ | Viscosity (Pa·s) |
| $\sigma_{pl}$ | Total stress tensor |
| $\alpha_B$ | Biot-Willis coefficient |
| $e_{\text{vol}}$ | Volumetric strain |
| $S_l$ | Liquid saturation |
| $P$ | Pressure (Pa) |
| $g$ | Acceleration of gravity |
| $\epsilon_p$ | Porosity |
| $\chi_f$ | Compressibility |
| $E$ | Young's modulus |
| $G$ | Modulus of rigidity |
| $v$ | Poisson's ratio |
| $D_c$ | Capillary diffusivity |
| $k_{\text{eff}}$ | Effective permeability |
| $D_{\text{eff}}$ | Diffusivity (m$^2$/s) |
| $X_v$ | Molar fraction |
| $P_v$ | Vapor pressure (Pa) |
| $P_g$ | Gas pressure (Pa) |
| $X_a$ | Molar fraction |
| $hm$ | Mass transfer coefficient (m/s) |
| $C_{v\infty}$ | Vapor concentration at the surface |
| $T_\infty$ | Air temperature (ºC) |
| $T_s$ | Atmosphere temperature (K) |
| $\rho_{a\infty}$ | Temperature of solid (K) |
| $P_\infty$ | Air density in the tunnel (kg/m$^3$) |
| $h_c$ | Atmosphere pressure (Pa)Volumetric strain |
| $h_m$ | Heat transfer coefficient (W/m$^2$ K) |
| $N$ | Mass transfer coefficient (m/s) |
| $S_z$ | Experimental data |
| $O_z$ | Predicted values |
| $\lambda_s$ | Experimental values |
| $\mu_s$ | Lamé's constant |
| $D$ | Modulus of shear |
| $e_{\text{vol}}$ | Diffusivity (m$^2$/s) |
| $h_c$ | Volumetric strain |
| $h_m$ | Heat transfer coefficient (W/m$^2$ K) |
| Subscripts | Mass transfer coefficient (m/s) |
| ***a*** | Air |
| $c$ | Capillary |
| eff | Effective |
| $f$ | Fluid |
| $g$ | Gas |
| AMS | Mass separating agent |

**Acknowledgements:** Authors acknowledge CONACYT for the scholarship 333436 for Perez-Santiago Angel (International mobility scholarship 486004), and to the Instituto Politécnico Nacional (Mexico) for SIP-IPN funding: Project ID code 20180678, 20195013, 20200285, and 20211251.

**Author contributions:** All the authors have accepted responsibility for the entire content of this submitted manuscript and approved submission.

**Research funding:** This research was funded by Instituto Politécnico Nacional (Mexico) under 20180678, 20195013, 20200285, and 20211251.

**Conflict of interest statement:** The authors declare no conflicts of interest regarding this article.

# References

1. Waldron KW, Smith AC, Parr AJ, Ng A, Parker ML. New approaches to understanding and controlling cell separation in relation to fruit and vegetable texture. Trends Food Sci Technol 1997;8: 213–21.
2. Kilcast D. Texture in food. Cambridge: Woodhead; 2004, vol. 2.
3. Huang Y, Whittaker AD, Lacey RE. Automation for food engineering: food quality quantization and process control. Boca Raton: CRC Press; 2001.
4. Maskan M. Drying, shrinkage and rehydration characteristics of kiwifruits during hot air and microwave drying. J Food Eng 2001; 48:177–82.
5. Raghavan GSV, Orsat V. Recent advances in drying of biomaterials for superior quality bioproducts. Asia Pac J Chem Eng 2007;2:20–9.
6. Datta AK, Halder A. Status of food process modeling and where do we go from here (Synthesis of the outcome from brainstorming). Compr Rev Food Sci Food Saf 2008;7:117–20.
7. Defraeye T, Radu A. Insights in convective drying of fruit by coupled modeling of fruit drying, deformation, quality evolution and convective exchange with the airflow. Appl Therm Eng 2018; 129:1026–38.
8. Piatnitski A, Ptashnyk M. Homogenization of biomechanical models of plant tissues with randomly distributed cells. Nonlinearity 2020;33:5510–42.
9. Xiao B, Chang J, Huang X, Liu X. A moisture transfer model for isothermal drying of plant cellular materials based on the pore network approach. Dry Technol 2014;32:1071–81.
10. Sandoval-Torres S, Allier-González AL. Linear and nonlinear drying behavior in tuberous crop slices. Dry Technol 2015;33: 559–69.
11. Itaya Y, Kobayashi T, Hayakawa K-I. Three-dimensional heat and moisture transfer with viscoelastic strain-stress formation in composite food during drying. Int J Heat Mass Transfer 1995;38: 1173–85.
12. Mayor L, Sereno AM. Modelling shrinkage during convective drying of food materials: a review. J Food Eng 2004;61: 373–86.
13. Fanta SW, Abera MK, Aregawi WA, Ho QT, Verboven P, Carmeliet J, et al. Microscale modeling of coupled water transport and mechanical deformation of fruit tissue during dehydration. J Food Eng 2014;124:86–96.
14. Dhall A, Datta AK. Transport in deformable food materials: a poromechanics approach. Chem Eng Sci 2011;66:6482–97.
15. Wang N, Brennan JG. A mathematical model of simultaneous heat and moisture transfer during drying of potato. J Food Eng 1995; 24:47–60.

16. Curcio S, Aversa M. Influence of shrinkage on convective drying of fresh vegetables: a theoretical model. J Food Eng 2014;123: 36–49.
17. Gulati T, Datta AK. Mechanistic understanding of case-hardening and texture development during drying of food materials. J Food Eng 2015;166:119–38.
18. Bonazzi C, Bimbenet J-J. Séchage des produits alimentaires-principes. Tech L'ingénieur 2003;Article number: F3002 v1.
19. Léonard A, Blacher S, Nimmol C, Devahastin S. Effect of far-infrared radiation assisted drying on microstructure of banana slices: an illustrative use of X-ray microtomography in microstructural evaluation of a food product. J Food Eng 2008;85: 154–62.
20. Rahman MM, Joardder MUH, Karim A. Non-destructive investigation of cellular level moisture distribution and morphological changes during drying of a plant-based food material. Biosyst Eng 2018;169:126–38.
21. Verboven P, Nemeth A, Abera MK, Bongaers E, Daelemans D, Estrade P, et al. Optical coherence tomography visualizes microstructure of apple peel. Postharvest Biol Technol 2013;78: 123–32.
22. Cantre D, East A, Verboven P, Trejo Araya X, Herremans E, Nicolaï BM, et al. Microstructural characterisation of commercial kiwifruit cultivars using X-ray micro computed tomography. Postharvest Biol Technol 2014;92:79–86.
23. Szadzińska J, Łechtańska J, Pashminehazar R, Kharaghani A, Tsotsas E. Microwave- and ultrasound-assisted convective drying of raspberries: drying kinetics and microstructural changes. Dry Technol 2019;37:1–12.
24. Cantre D, Herremans E, Verboven P, Ampofo-Asiama J, Nicolaï B. Characterization of the 3-D microstructure of mango (Mangifera indica L. cv. Carabao) during ripening using X-ray computed microtomography. Innovat Food Sci Emerg Technol 2014;24:28–39.
25. Szadzińska J, Mierzwa D, Pawłowski A, Musielak G, Pashminehazar R, Kharaghani A. Ultrasound- and microwave-assisted intermittent drying of red beetroot. Dry Technol 2020; 38:93–107.
26. Madiouli J, Sghaier J, Orteu J-J, Robert L, Lecomte D, Sammouda H. Non-contact measurement of the shrinkage and calculation of porosity during the drying of banana. Dry Technol 2011;29: 1358–64.
27. Vicent V, Verboven P, Ndoye F-T, Alvarez G, Nicolaï B. A new method developed to characterize the 3D microstructure of frozen apple using X-ray micro-CT. J Food Eng 2017;212:154–64.
28. Alam T, Takhar PS. Microstructural characterization of fried potato disks using X-ray micro computed tomography. J Food Sci 2016;81:E651–64.
29. Ahn JY, Kil DY, Kong C, Kim BG. Comparison of oven-drying methods for determination of moisture content in feed ingredients. Asian-Australas J Anim Sci 2014;27:1615–22.
30. Leonard A, Blacher S, Marchot P, Crine M. Use of X-ray Microtomography to follow the convective heat drying of wastewater sludges Dry Technol 2002;20:1053–69.
31. Leonard A, Blacher S, Marchot P, Crine M. Use of X-ray microtomography to follow the convective heat drying of wastewater sludges. Dry Technol 2002;20:1053–69.
32. Niklas K. Plant biomechanis: an engineering approach to plant form and function. Chicago: The University of Chicago Press; 1992:607 p.
33. Walstra P. Physical chemistry of foods. Boca Raton: Taylor & Francis Inc. CRC Press; 2002:832 p.
34. Halder A, Datta AK, Spanswick RM. Water transport in cellular tissues during thermal processing. AIChE J 2011;57:2574–88.
35. Datta AK. Biological and bioenvironmental heat and mass transfe. New York: Marcel Dekker; 2002:424 p.
36. Sandoval-Torres S, Pérez-Santiago A, Hernández-Bautista E. Drying model for softwood and moisture patterns measured by magnetic resonance imaging. Dry Technol 2019;37:458–67.
37. Yang H, Sakai N. Shrinkage and mechanical characteristics of potato undergoing air convection drying. Japan J Food Eng 2001; 2:67–72.
38. Grotte M, Duprat F, Piétri E, Loonis D. Young's modulus, Poisson's ratio, and lame's coefficients of golden delicious apple. Int J Food Prop 2002;5:333–49.
39. Wang N, Brennan JG. Thermal conductivity of potato as a function of moisture content. J Food Eng 1992;17:153–60.
40. Srikiatden J, Roberts JS. Predicting moisture profiles in potato and carrot during convective hot air drying using isothermally measured effective diffusivity. J Food Eng 2008;84:516–25.
41. Siebel J. Specific heat of various products. Ice and refrigeration. Boca Raton: CRC Press; 1982:256 p.
42. Plawsky JL. Transport phenomena fundamentals. Boca Raton: CRC Press; 2014:345 p.
43. Turner I. A two dimensional orthotropic model for simulating wood drying processe. Appl Math Model 1996;20:60–81.
44. Yang H, Sakai N, Watanabe M. Drying model with non-isotropic shrinkage deformation undergoing simultaneous heat and mass transfer. Dry Technol 2001;19:1441–60.
45. Le KH, Tsotsas E, Kharaghani A. Continuum-scale modeling of superheated steam drying of cellular plant porous media. Int J Heat Mass Tran 2018;124:1033–44.
46. Rao MA. Rheology of fluid, semisolid, and solid foods, Food engineering series. Boston, MA: Springer US; 2014:461 p.
47. Finney EE, Hall CW. Elastic properties of potatoes. Trans ASAE (Am Soc Agric Eng) 1967;10:0004–8.
48. Srivastava V, Chester SA, Ames NM, Anand L. A thermo-mechanically-coupled large-deformation theory for amorphous polymers in a temperature range which spans their glass transition. Int J Plast 2010;26:1138–82.
49. Srikiatden J, Roberts JS. Moisture transfer in solid food materials: a review of mechanisms, models, and measurements. Int J Food Prop 2007;10:739–77.
50. Hassini L, Azzouz S, Peczalski R, Belghith A. Estimation of potato moisture diffusivity from convective drying kinetics with correction for shrinkage. J Food Eng 2007;79:47–56.
51. Witrowa-Rajchert D, Rząca M. Effect of drying method on the microstructure and physical properties of dried apples. Dry Technol 2009;27:903–9.
52. Oey ML, Vanstreels E, De Baerdemaeker J, Tijskens E, Ramon H, Hertog MLATM, et al. Effect of turgor on micromechanical and structural properties of apple tissue: a quantitative analysis. Postharvest Biol Technol 2007;44:240–7.